Progress in PHOTOVOLTAICS

PROGRESS IN PHOTOVOLTAICS: RESEARCH AND APPLICATIONS
Prog. Photovolt: Res. Appl. (2014)
Published online in Wiley Online Library (wileyonlinelibrary.com). DOI: 10.1002/pip.2506

RESEARCH ARTICLE

An effective way to simultaneous realization of excellent optical and electrical performance in large-scale Si nano/microstructures

Zengguang Huang[1,2], Sihua Zhong[1], Xia Hua[1], Xingxing Lin[1], Xiangyang Kong[3], Ning Dai[4] and Wenzhong Shen[1]*

[1] Laboratory of Condensed Matter Spectroscopy and Opto-Electronic Physics, and Key Laboratory of Artificial Structures and Quantum Control (Ministry of Education), Department of Physics, and Institute of Solar Energy, Shanghai Jiao Tong University, Shanghai 200240, China
[2] School of Science, Huaihai Institute of Technology, Lianyungang 222005, Jiangsu Province, China
[3] School of Materials Science and Engineering, Shanghai Jiao Tong University, Shanghai 200240, China
[4] National Laboratory for Infrared Physics, Shanghai Institute of Technical Physics, Chinese Academy of Sciences, Shanghai 200083, China

ABSTRACT

Despite the optical advantage of near-zero reflection, the silicon nanowire arrays (SiNWs)-based solar cells cannot yet achieve satisfactory high efficiency because of the serious surface recombination arising from the greatly enlarged surface area. The trade-off between reflection and recombination fundamentally prevents the conventional SiNWs structure from having both minimal optical and electrical losses. Here, we report the simultaneous realization of the best optical anti-reflection (the solar averaged reflectance of 1.38%) and electrical passivation (the surface recombination velocity of 44.72 cm/s) by effectively combining the Si nano/microstructures (N/M-Strus) with atomic-layer-deposition (ALD)-Al_2O_3 passivation. The composite structures are prepared on the pyramid-textured Si wafers with large-scale $125 \times 125\ mm^2$ by the two-step metal-assisted chemical etching method and the thermal ALD-Al_2O_3 treatment. Although the excellent optical anti-reflection is observed because of the complementary contribution of Si N/M-Strus at short wavelength and ALD-Al_2O_3 at long wavelength, the low recombination has also been realized because the field effect passivation is enhanced for the longer and thinner SiNWs through the more effective suppression of the minority carrier movement and the reduction of the pure-pyramid-textured surface recombination. We have further numerically modeled the Al_2O_3-passivated Si N/M-Strus-based solar cell and obtain the high conversion efficiency of 21.04%. The present work opens a new way to realize high-efficiency SiNWs-based solar cells.

KEYWORDS

silicon nanowires; large scale; atomic layer deposition; Al_2O_3; field effect passivation; minority carrier lifetime

***Correspondence**

Wenzhong Shen, Laboratory of Condensed Matter Spectroscopy and Opto-Electronic Physics, and Key Laboratory of Artificial Structures and Quantum Control (Ministry of Education), Department of Physics, and Institute of Solar Energy, Shanghai Jiao Tong University, Shanghai 200240, China.
E-mail: wzshen@sjtu.edu.cn

Received 3 December 2013; Revised 5 March 2014; Accepted 25 March 2014

1. INTRODUCTION

Over the past few years, vertically aligned silicon nanowire arrays (SiNWs) have attracted substantial interests, because of the ultralow reflection over a broad range of incident angles [1,2] and a promising application to the high-performance solar cells at low cost [3–8]. The excellent anti-reflection of SiNWs is due to the formation of the density-graded layer with features smaller than the wavelength of light or the increase of the path length for the surface features larger than the wavelength of light [9–11]. Unfortunately, despite the excellent optical advantages, the SiNWs-based solar cells show yet unsatisfied energy conversion efficiencies (η) because of the serious surface recombination arising from the concomitant high surface–volume ration. Many research groups have carried out many beneficial tries to minimize the optical and electrical losses and have indeed made great progresses in the performance of SiNWs-based

solar cells [12–25]. Oh *et al.* [26] have reported an 18.2% efficient nanostructure black Si solar cell through controlling the front surface area and Auger recombination. However, the improvement of these solar cells implies a fact that the high η requires the short nanostructure length, because of the careful balance between the reflection and the photo-carrier recombination. In other words, the minimum optical and electrical losses cannot be simultaneously achieved in these Si-nanostructure-based solar cells.

It is well known that the surface passivation plays a crucial role in improving cell performance by reducing the surface recombination. Thermal oxidation, carbon thin films, and chlorine dielectric treatments have been widely studied in SiNWs-based solar cells [16,27,28]; however, these processes offer limited improvement because they merely provide the chemical passivation through saturating the dangling bonds. Another treatment of atomic-layer-deposition (ALD)-Al_2O_3 thin film not only yields the excellent chemical passivation but also results in a strong field effect passivation because of the fixed charges carried by the interface of Si/Al_2O_3, which can substantially reduce the surface recombination velocity (SRV) [29–34]. In the ALD-Al_2O_3-passivated *n*-type planar Si, Wang *et al.* [35] have reported a low density of the interface traps of ~1.8×10^{11} cm^{-2}/eV and a high fixed charge density of approximately -3×10^{12} cm^{-2}, which indicate the good chemical and field effect passivation, respectively. Saint-Cast *et al.* [36] achieved an η of 21.3% by applying the ALD-Al_2O_3 thin film to the rear surface of the *p*-type passivated emitter and rear cell (with the area 20×20 mm^2).

In this paper, we report the realization of both increasing effective minority carrier lifetime and reducing reflectance with the increase of SiNWs length, which guarantees the simultaneous achievement of the best optical (the lowest solar averaged reflectance of 1.38%) and electrical (the lowest SRV of 44.72 cm/s) performance. The success lies in a combination of the ALD-Al_2O_3 with the compound Si nano/microstructures (N/M-Strus) consisting of nanoscale SiNWs and microscale pyramid texture. The composite structure exhibits the stronger field effect passivation for the longer and thinner SiNWs and the reduced pure-pyramid-textured surface recombination, together with a complementary anti-reflection characteristic of the Si N/M-Strus at the short wavelength and the ALD-Al_2O_3 at the long wavelength. The output performance of the Al_2O_3-passivated Si N/M-Strus-based solar cells is simulated by PC1D software, and the highest η reaches up to 21.04%.

2. EXPERIMENT AND STRUCTURE

Figure 1(a) presents the main synthesis process of Al_2O_3-passivated Si N/M-Strus through the two-step metal-assisted chemical etching (MACE) method and ALD-Al_2O_3 treatment. First, the solar grade *p*-type (100) Czochralski-Si (Cz-Si) wafers (resistivity ~2 Ωcm, thickness ~180 μm, and a large-scale 125×125 mm^2 with a pyramid texture) were cleaned in acetone and alcohol by ultrasonic washing for 30 min, respectively, and then immersed in 5% (volume

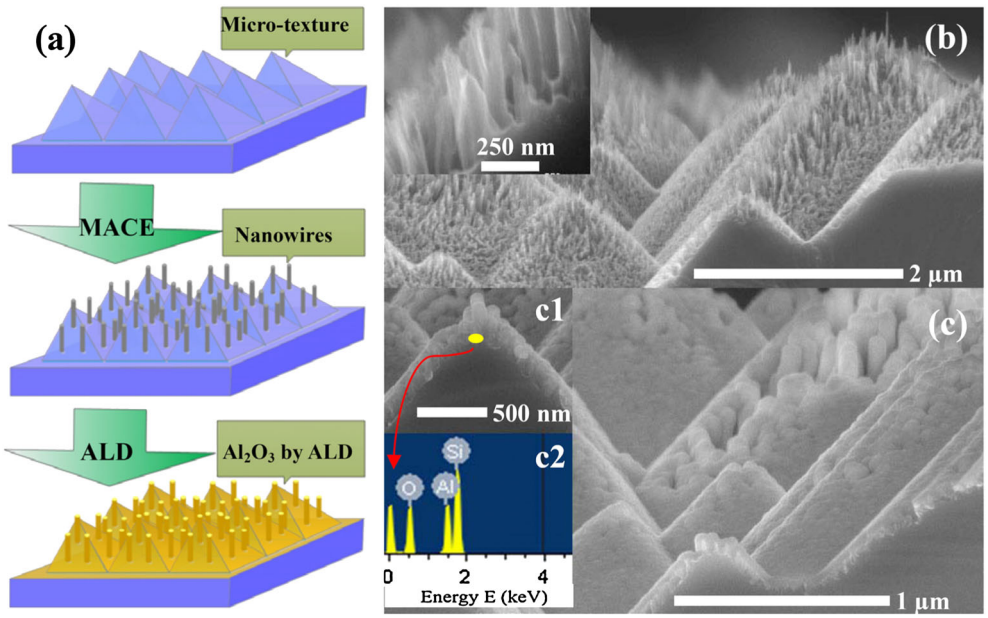

Figure 1. Process flow and SEM characterization of Si N/M-Strus. (a) The flow schematic diagram of the preparing process. (b) The oblique-view SEM image of as-prepared Si N/M-Strus. Inset is the high magnitude SEM image of SiNWs on the facet of microscale pyramid texture. (c) The oblique-view SEM image of the ALD-Al_2O_3-coated Si N/M-Strus. Inset c1 is high magnitude SEM image of NWs conformal coated by Al_2O_3 thin film. Inset c2 is the EDS of the yellow elliptical area as shown in inset c1.

ratio) HF for 1 min to remove the natural oxide layer. Second, the Si N/M-Strus were fabricated on these wafers by the two-step MACE method [13] as follows: in the first step, the assisted Ag^+ particle clusters were deposited onto the sample surface by immersing the cleaned wafers in the 5 M HF/0.02 M $AgNO_3$ fixed solution for 90 s; in the second step, the as-deposited samples with Ag^+ particle clusters were etched in the 5 M HF/0.01 M H_2O_2 fixed solution for 100–600 s to form the SiNWs with different lengths. After the MACE treatment, the residual impurities were wiped off from the surface of SiNWs by immersing the samples in 1:1 HNO_3/H_2O (volume ratio) solution for 30 min at room temperature, followed by rinsing with excess copious deionized water. Subsequently, the different thickness Al_2O_3 thin films were deposited on the surface of the as-prepared N/M-Strus samples through the reaction of trimethylaluminum and ozone at 185 °C and 3 mbar using the thermal ALD method (TFS 200, Beneq, Finland). Finally, all samples were annealed in the atmosphere ambient at 425 °C for 5 min [37] (Thermolyne, Thermo Scientific, Waltham, MA, USA), in order to activate the optimal passivation effect of ALD-Al_2O_3.

The morphologies of the Si N/M-Strus and element distribution were investigated by field emission scanning electron microscopy (SEM, FEI Sirion 200) and the energy dispersive X-ray spectroscopy (EDS). The optical reflectance spectra were obtained on the station of quantum efficiency measurement (QEX10, PV Measurements, Boulder, Co, USA). The effective minority carrier lifetimes were measured by using the mapping mode of microwave photoconductance method with a 904 nm wavelength laser and an average injection concentration $\Delta n = 4.81 \times 10^{14}\,\mathrm{cm}^{-3}$ (WT-2000, Semilab, Billerica, MA, USA).

We divided the samples into four series (A, B, C, and D) corresponding to the different etching times 100, 250, 400, and 600 s, respectively, which yielded the SiNWs length ~180, 550, 870, and 1200 nm. Among each series, we used the number of ALD cycles, that is, 100, 250, 400, 500, and 700, to characterize the different Al_2O_3 thickness on the Si N/M-Strus (note that one ALD cycle can form ~0.1-nm-thick Al_2O_3 evaluated from the self-limiting reaction characteristics of ALD method). Hence, we could denote a sample of a certain series by combing a capital letter with the number of ALD cycles, for example, D-250 means series D (SiNWs length ~1200 nm) with 250 ALD cycles (Al_2O_3 thickness ~25 nm).

Figure 1(b) illustrates the oblique-view SEM image of the Si N/M-Strus for series B consisting of the nanoscale SiNWs along <100> crystal axis [38] and microscale pyramid texture whose facets normal is along <111> oriented direction, and the inset is the corresponding high magnitude cross-sectional imagine of SiNWs. The average length of NWs is ~550 nm, and the diameter is in the range 70–80 nm. Figure 1(c) shows an oblique-view SEM figure of the Al_2O_3-coated (400 ALD cycles) surface of SiNWs for series A. We can find that the ALD-Al_2O_3 thin film (thickness ~40 nm) is homogeneous and conformal (see the inset c1), which benefits from the self-limiting gas–solid reaction between the precursors and substrate. We also give out the EDS result of the yellow area in inset c1 (see inset c2), indicating that the atom percent content of oxygen, aluminum, and Si are 67.65%, 10.61%, and 21.74%, respectively.

3. ANTI-REFLECTION PERFORMANCE

Figure 2(a) shows the experimentally obtained reflectance R_{ave} of the naked N/M-Strus under different etching times (i.e., A-0, B-0, C-0, and D-0). Note that the solar averaged reflectance R_{ave} here is calculated by averaging the reflectance over the AM1.5 spectrum in the wavelength range 300–1100 nm as follows:

$$R_{ave} = \frac{\int_{300\ nm}^{1100\ nm} R(\lambda)\cdot S(\lambda)\cdot d\lambda}{\int_{300\ nm}^{1100\ nm} S(\lambda)\cdot d\lambda} \quad (1)$$

where $R(\lambda)$ and $S(\lambda)$ denote the measured reflectance and AM1.5 solar photon spectral distribution, respectively. The SiNWs lengths obtained from SEM images are also indicated, which show an approximate linear increase with the etching time. We can see that the R_{ave} of these naked N/M-Strus illustrates a contrary trend compared with the SiNWs length, implying that longer SiNWs clearly offer better light trapping effect, which matches well with the results in the literature [38]. Figure 2(b) further presents the reflectance spectra of the four series and the pure-pyramid-textured sample. Obviously, the reflectance is greatly suppressed through the entire spectra compared with that of the pyramid-textured surface, and the anti-reflection performance is even better for longer SiNWs. Actually, the reflectance in short wavelength range 300–600 nm shows much more significant improvement than that in long wavelength 900–1100 nm, which can be attributed to the fact that the sizes of the SiNWs are comparable with the short wavelengths [25].

Next, we turn to illustrate the anti-reflection effect of the Al_2O_3-coated Si N/M-Strus through the reflectance spectra of series D with different ALD cycles as shown in Figure 2(c). The solar averaged reflectance R_{ave} of D-0, D-250, D-400, and D-500 are calculated as 6.49%, 2.63%, 1.74%, and 1.94%, respectively, presenting that D-400 owns the best anti-reflection performance. It should be noted that for the long wavelength (>600 nm), the reflectance of D-250, D-400, and D-500 are greatly reduced compared with the D-0. This is very important because the excellent anti-reflection behavior of the ALD-Al_2O_3 thin film can complement the drawback of the naked SiNWs in the long wavelength range. As a result, combining the SiNWs with the ALD-Al_2O_3 thin film may be a promising design to realize excellent light trapping because of the anti-reflection effect both for short and long wavelength region.

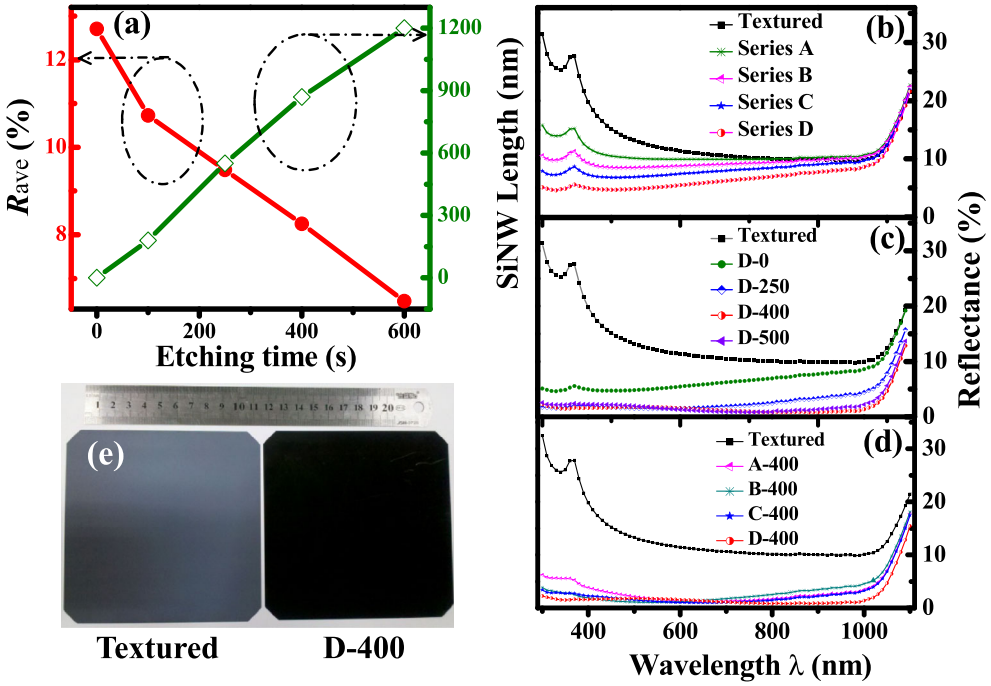

Figure 2. (a) SiNWs length (right) and the solar averaged reflectance R_{ave} (left) of naked Si N/M-Strus with respect to etching time. (b) Reflectance spectra of series A (olive), B (magenta), C (blue), D (red), and pyramid-textured sample (black). (c) Reflectance spectra of D-0 (olive), D-250 (blue), D-400 (red), and D-500 (violet). (d) Reflectance spectra of A-400 (magenta), B-400 (olive), C-400 (blue), and D-400 (red). (e) Photograph of D-400 and pyramid-textured wafer.

We further apply the best 400 ALD cycles as discussed earlier to all four series (i.e., A-400, B-400, C-400, and D-400) and present the reflectance spectra in Figure 2(d). We can find that all series exhibit a substantial decline of the reflectance compared with the SiNWs without coating (Figure 2(b)), and the descending trend with the increment of SiNWs lengths is very similar as well. Among the four series, the D-400 possesses an ultralow solar averaged reflectance of 1.38% in the most important wavelength region 300–900 nm where c-Si solar cells work effectively, which is mainly distributed to the ultralow solar averaged reflectance of 1.64% in the short wavelength range 300–450 nm and 0.85% in long wavelength range 800–900 nm. It is worth noting, comparing with the poor short-wavelength anti-reflection of traditional c-Si solar cells, the D-400 has reduced the absolute solar averaged reflectance by 7.86% in the wavelength range 300–450 nm, which addresses great potential for advanced photovoltaic devices. Finally, we also give out in Figure 2(e) the photograph of black D-400 and the pyramid-textured wafer for comparison (with a large-scale $125 \times 125\ \mathrm{mm}^2$).

4. FIELD EFFECT PASSIVATION AND APPLICATION

Although the ALD-Al_2O_3-coated Si N/M-Strus manifest an excellent optical performance, a low surface recombination is also necessarily required to achieve outstanding electrical properties [19–24] for high-efficiency Si N/M-Strus-based photovoltaic or photoelectric devices. Consequently, we study the passivation effect of the ALD-Al_2O_3, which indicates the ability to suppress the surface recombination and can be characterized by the minority carrier lifetime. Generally, the effective minority carrier lifetime τ_{eff} can be expressed as

$$\frac{1}{\tau_{eff}} = \frac{1}{\tau_{bulk}} + \frac{S_{eff}^{F} + S_{eff}^{B}}{d} \tag{2}$$

where τ_{bulk} is the bulk Shockley–Read–Hall lifetime, S_{eff}^{F} and S_{eff}^{B} denote the effective SRV at the front and back surfaces, respectively, and d is the wafer thickness (in our case, $d = 180\ \mu\mathrm{m}$). To investigate the effect of the high surface area on the S_{eff}^{F} of Si nanostructure, an expression for the measured τ_{eff} is proposed [26] as

$$\frac{1}{\tau_{eff}} = \frac{1}{\tau_{bulk}} + \frac{A^{F}}{A} \cdot S_{loc}^{F} \cdot \frac{1}{d} + \frac{S_{eff}^{B}}{d} \tag{3}$$

where $S_{loc}^{F} \cdot (A^{F}/A) = S_{loc}^{F} \cdot \alpha = S_{eff}^{F}$. Here, S_{loc}^{F} denotes the local effective SRV at and very near the actual front surface of Si nanostructure, and $\alpha = A^{F}/A$ is the surface area enhancement factor with A^{F} being the N/M-Strus front surface area including both the total lateral area of SiNWs and the pure-pyramid-textured surface area A. By using the length,

diameter, and the areal density of SiNWs obtained from the SEM images, α of series A, B, C, and D can be evaluated as 2.25, 4.31, 5.86, and 7.17, respectively. Figure 3(a) shows that α keeps approximately proportional to the SiNWs length (right) and the unpassivated Si N/M-Strus with the larger α has the lower τ_{ave} (the average value of τ_{eff} in mapping area, left), suggesting a more serious surface recombination, which matches well with our previous work [24].

Figure 3(b) demonstrates a systematic study on the τ_{ave} of all series with different ALD cycles, under the case of one-side passivation. We can clearly find that the τ_{ave} of all passivated series greatly increase by at least one order of magnitude compared with the corresponding unpassivated counterparts (0 ALD cycles). Besides, the τ_{ave} shows a fluctuating trend with increasing ALD cycles and reaches the best τ_{ave} at 400 ALD cycles for all four series, among which the D-400 has the highest value of 33.23 µs. When the ALD cycles become 700, the τ_{ave} of all series is observed to substantially reduce because of the blistering effect in an excess thick ALD-Al_2O_3 layer [39]. Moreover, it is of great significance that the τ_{ave} exhibits a notable increment with the increase of α (corresponding to the increasing SiNWs length less than 1200 nm) for the fixed ALD cycles 100, 250, or 400 (framed by the dashed-line ellipse), which is a very novel electrical characteristic and acts totally contrary to the regular SiNWs [25,26]. This unique new finding indicates that the longer SiNWs (less than 1200 nm) can support lower surface recombination, opening a new way to simultaneously realize both the minimal optical and electrical losses [22–26].

In order to quantify the low surface recombination brought by the novel electrical characteristic, we also explore the minority carrier lifetimes of the both-side passivated series ($S_{eff}^{F} = S_{eff}^{B}$) in Figure 3(c) with the same 400 ALD cycles. The τ_{ave} of the both-side passivated series arises along with the increase of α, which is consistent with the one-side passivated case shown in Figure 3(b). The D-400 yields the highest τ_{ave} of 55.90 µs, whereas the τ_{max} (the maximum value of τ_{eff} in mapping area) of the D-400 even reaches up to 85.94 µs. According to Equation (3), the SRVs corresponding to the τ_{max} of the both-side passivated series are calculated to be 236.63, 118.43, 81.35, and 44.72 cm/s, respectively, as shown in Figure 3(d) (τ_{bulk} = 150.0 µs for our low-quality solar grade *p*-type Cz-Si wafer with thickness ~180 µm). We can see that the SRVs of these series decline with the increase of α, while the D-400 achieves the best SRV of 44.72 cm/s, which is extremely low benefiting from the largest τ_{eff} under longest SiNWs. With the help of the Corona charge–voltage property (from Semilab PV-2000), we obtain the flat band voltage of 2.153 V for the optimal ALD-Al_2O_3-passivated Si N/M-Strus (D-400). According to the relationship between the fixed charge density and the flat band voltage in the oxide/semiconductor structure [40], the fixed charge density in the combined

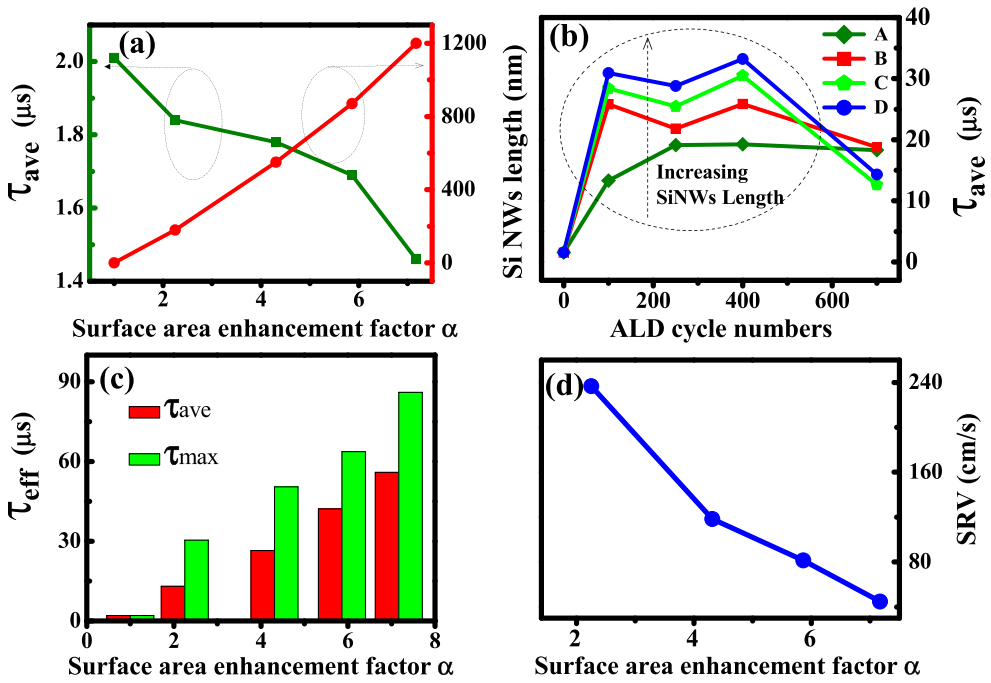

Figure 3. (a) SiNWs length (red) and τ_{ave} (olive) of unpassivated N/M-Strus with respect to surface area enhancement factor α. (b) The effect of different ALD cycles on the average τ_{eff} for series A (olive), B (red), C (green), and D (blue). (c) Column diagram of τ_{max} (green) and τ_{ave} (red) with respect to α (all series with the same 400 ALD cycles). (d) The SRV (corresponding to τ_{max}) with respect to α (four series with the same 400 ALD cycles).

structure can be calculated to be $-3.09\times10^{12}\,cm^{-2}$, which indicates a strong field effect passivation and is fully consistent with the references [35,41].

In order to provide an insight into the relationship between the field effect passivation and the novel characteristic (the longer and thinner SiNWs possess the lower SRV), we have further studied the influence of the morphologic variation of the Si N/M-Strus on the field effect passivation. Figure 4(a) reveals that the surface morphology of the Si N/M-Strus varies with the etching time. The corresponding cross-sectional schematic drawings (series A, B, C, and D) are shown below to better understand this evolution. We can see that with the increase of etching time the SiNWs will be longer and thinner, while the pure-pyramid-textured surfaces (framed by dashed-line triangles) become smaller. As is discussed earlier, the ALD-Al_2O_3 field effect passivation is determined by the fixed charges that repel the minority carriers away from the surface; thus, the level of the field effect passivation can be described by the minority carrier density (MCD) in the neighborhood of the surface. Figure 4(b) presents the influence of SiNWs diameter on the distribution of MCD simulated by PC1D software, which usually simulates the semiconductor devices by solving the quasi-one-dimensional transport equations of electrons and holes. Note that the SiNW is equivalently simulated by setting the layer as thick as the diameter of SiNW, and the constant fixed charge density is set as $-3.09\times10^{12}\,cm^{-2}$ for the four series with 400 ALD cycles. We see that the Gaussian distribution of MCDs in Al_2O_3-passivated

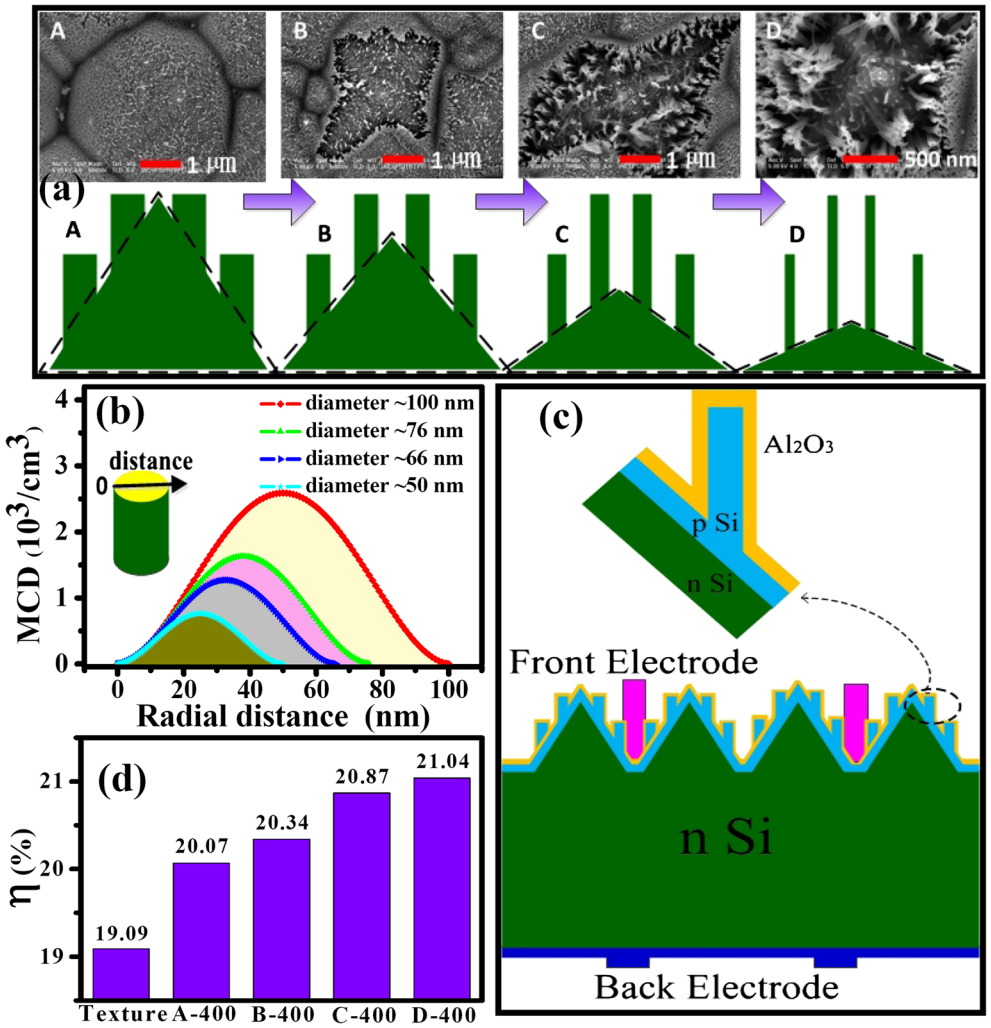

Figure 4. (a) SEM images and the corresponding schematics with increasing etching time 100 (series A), 250 (series B), 400 (series C), and 600 s (series D), together with the pure-pyramid-textured surface framed by dashed-line triangles. (b) Distribution of the MCD with respect to the radial distance obtained by PC1D software (the fixed charge density $-3.09\times10^{12}\,cm^{-2}$, the doping concentration of bulk Si ~$1\times10^{16}\,cm^{-3}$). *X* axis "radial distance" denotes the distance from one point on SiNWs surface to another point in SiNWs along with the radial direction (see inset). (c) Schematic of the Si N/M-Strus-based solar cell. (d) Column diagram of η for the four series Si N/M-Strus-based solar cells and the pure-pyramid-textured counterpart by PC1D software (see the detailed parameters in Table I).

Table I. The detailed input parameters and simulation results for the Si N/M-Strus-based solar cells with the area of $125 \times 125\,mm^2$, together with the pyramid-textured solar cell as reference.

	V_{oc} (V)	I_{sc} (A)	*FF* (%)	η (%)	R_{ave} (%)	SRV (cm/s)	τ_{ave} (μs)
Textured	0.650	5.912	77.61	19.09	12.71	4417.60	2.010
A-400	0.653	6.101	78.72	20.07	2.64	630.77	13.029
B-400	0.655	6.150	78.90	20.34	2.52	406.93	19.275
C-400	0.658	6.238	79.45	20.87	2.12	153.48	42.195
D-400	0.659	6.264	79.64	21.04	1.74	101.02	55.895

R_{ave}, SRV and τ_{ave} are extracted from experiments, and the other relevant input parameters for all series are the same and from actual data of the production line: the sheet resistance of the emitter is about 80 Ω/sq; the doping concentration of *n*-type base region and *p*-type emitter are 1.07×10^{16} and $2.79 \times 10^{20}\,cm^{-3}$, respectively; $\tau_{bulk,n}$ and $\tau_{bulk,p}$ are 1000 and 150 μs, respectively; the series resistance is $1.5 \times 10^{-3}\,\Omega$; and the fixed charge density is $-3.09 \times 10^{12}\,cm^{-2}$.

SiNWs with the diameter 100 nm (length ~180 nm), 76 nm (length ~550 nm), 66 nm (length ~870 nm), and 50 nm (length ~1200 nm) reaches the peak values of 2.6×10^3, 1.6×10^3, 1.2×10^3, and $0.7 \times 10^3\,cm^{-3}$ at the SiNWs center, respectively. Clearly, the peak values of MCDs rapidly decline with the decrease of SiNWs diameter (corresponding to the increase of SiNWs length), and all these peak values are far less than the uniform distribution of $1.04 \times 10^4\,cm^{-3}$ (the doping concentration of bulk Si $\sim 1 \times 10^{16}\,cm^{-3}$) in the unpassivated SiNWs. The lower MCD indicates that the thinner SiNWs (corresponding to longer SiNWs) with the constant fixed charges can more effectively prevent the minority carriers from bulk Si moving into the SiNWs, that is, a better field effect passivation for the longer and thinner SiNWs. Moreover, the pure-pyramid-textured surface area also decreases with increasing etching time, and thus its surface recombination lowers. As a result, the D-400 with the longest SiNWs demonstrates the lowest SRV, because of the strongest field effect passivation for the thinnest SiNWs and the smallest pure-pyramid-textured surface recombination.

The novel characteristic of this composite structure provides a feasible solution to simultaneously achieve both the minimum optical and electrical losses, revealing great potential applications to the high-performance solar cells, photoelectric detectors, or other photoelectric devices. Here, we design a Si N/M-Strus-based solar cell consisting of the *n*-type base region, the *p*-type emitter, and a conformal Al_2O_3 dielectric layer (Figure 4(c)). The upper enlarged view shows the construction of Al_2O_3-passivated *p–n* junction, especially the *p*-type emitter consisting of the whole SiNWs and the thin layer of pyramid facets. Figure 4(d) presents the output performance of the designed solar cell simulated by the PC1D software. Although the Si N/M-Strus-based solar cell cannot be constructed from PC1D software, we obtain the cell performance by equivalently simulating planar solar cells with the reflectance and the SRV extracted from the Al_2O_3-passivated Si N/M-Strus. Also, the detailed input parameters are obtained from actual data of the production line (Table I), which further guarantees the reliability and accuracy of the simulation. It is clear that the η of the Si N/M-Strus-based solar cell manifests a considerable increment with the increasing SiNWs, and the D-400 solar cell possesses the highest η of 21.04% that has increased by an absolute value of 1.95% more than that of the traditional pyramid-textured counterpart. Particularly, the D-400 solar cell yields an ultrahigh short-circuit current density of $40.09\,mA/cm^2$ (short-circuit current 6.26 A in $125 \times 125\,mm^2$), an open-circuit voltage of 0.659 V, and a fill factor of 0.796.

5. CONCLUSIONS

In conclusion, the ALD-Al_2O_3-passivated Si N/M-Strus formed on large-scale Si wafer by the two-step MACE method and ALD-Al_2O_3 treatment have been shown to simultaneously realize the best optical anti-reflection and electrical passivation for SiNWs-based solar cells. We find that not only the optical reflection can be suppressed to extremely low levels (the solar averaged reflectance of 1.38%) because of the complementary contribution of Si N/M-Strus at short wavelength and ALD-Al_2O_3 at long wavelength but also the electrical recombination can remain at a very low level (the SRV of 44.72 cm/s) because the longer and thinner SiNWs present lower surface recombination. This unique abnormal decrease of surface recombination with the increasing SiNWs length can be attributed to the stronger field effect passivation for the longer and thinner SiNWs and the reduced pure-pyramid-textured surface recombination and can play a crucial role to achieve the excellent electrical properties in addition to the ultralow reflection in SiNWs. Furthermore, we have simulated the Al_2O_3-passivated Si N/M-Strus-based solar cell and obtain the high conversion efficiency of 21.04%. This work breaks the limits of the trade-off between optical and electrical losses in the SiNWs and opens a potential approach to realize high-efficiency SiNWs-based solar cells.

ACKNOWLEDGEMENTS

This work was supported by the National Major Basic Research Project (2012CB934302) and the Natural Science Foundation of China (11174202 and 61234005).

REFERENCES

1. Koynov S, Brandt MS, Stutzmann M. Black nonreflecting silicon surfaces for solar cells. *Applied Physics Letters* 2006; **88**: 203107-1–203107-3.
2. Branz HM, Yost VE, Ward S, Jones KM, To B, Stradins P. Nanostructured black silicon and the optical reflectance of graded-density surfaces. *Applied Physics Letters* 2009; **94**: 231121-1–231121-3.
3. Tian B, Zheng X, Kempa T, Fang Y, Yu N, Yu G, Huang J, Lieber C. Coaxial silicon nanowires as solar cells and nanoelectronic power sources. *Nature* 2007; **449**: 885–888.
4. Hu L, Chen G. Analysis of optical absorption in silicon nanowire arrays for photovoltaic applications. *Nano Letters* 2007; **7**: 3249–3252.
5. Kempa TJ, Tian B, Kim DR, Hu J, Zheng X, Lieber CM. Single and tandem axial *p-i-n* nanowire photovoltaic devices. *Nano Letters* 2008; **8**: 3456–3460.
6. Stelzner T, Pietsch M, Andra G, Falk F, Ose E, Christiansen S. Silicon nanowire-based solar cells. *Nanotechnology* 2008; **19**: 295203-1–295203-4.
7. Yuan G, Zhao H, Liu X, Hasanali ZS, Zou Y, Levine A, Wang D. Synthesis and photoelectrochemical study of vertically aligned silicon nanowire arrays. *Angewandte Chemie International Edition* 2009; **121**: 9860–9864.
8. Peng KQ, Lee ST. Silicon nanowires for photovoltaic solar energy conversion. *Advanced Materials* 2011; **23**: 198–215.
9. Garnett E, Yang P. Light trapping in silicon nanowire solar cells. *Nano Letters* 2010; **10**: 1082–1087.
10. Kelzenberg MD, Boettcher SW, Petykiewicz JA, Turner-Evans DB, Putnam MC, Warren EL, Spurgeon JM, Briggs RM, Lewis NS, Atwater HA. Enhanced absorption and carrier collection in Si wire arrays for photovoltaic application. *Nature Materials* 2010; **9**: 239–244.
11. Han SE, Chen G. Optical absorption enhancement in silicon nanohole arrays for solar photovoltaics. *Nano Letters* 2010; **10**: 1012–1015.
12. Kayes BM, Atwater HA, Lewis NS. Comparison of the device physics principles of planar and radial *p-n* junction nanorod solar cells. *Journal of Applied Physics* 2005; **97**: 114302-1–114302-11.
13. Peng KQ, Xu Y, Wu Y, Yan YJ, Lee ST, Zhu J. Aligned single-crystalline Si nanowire arrays for photovoltaic applications. *Small* 2005; **1**: 1062–1067.
14. Fang H, Li XD, Song S, Xu Y, Zhu J. Fabrication of slantingly-aligned silicon nanowire arrays for solar cell application. *Nanotechnology* 2008; **19**: 255703-1–255703-6.
15. Shu Q, Wei J, Wang K, Zhu H, Li Z, Jia Y, Gui X, Guo N, Li X, Ma C, Wu D. Hybrid heterojunction and photoelectrochemistry solar cell based on silicon nanowires and double-walled carbon nanotubes. *Nano Letters* 2009; **9**: 4338–4342.
16. Yuan HC, Yost VE, Page MR, Stradins P, Meier DL, Branz HM. Efficient black silicon solar cell with a density-graded nanoporous surface: optical properties, performance limitations, and design rules. *Applied Physics Letters* 2009; **95**: 123501-1–123501-3.
17. Naughton M, Kempa K, Ren Z, Gao Y, Rybczynski J, Argenti N, Gao W, Wang Y, Peng Y, Naughton J, McMahon G, Paudel T, Lan Y, Burns M, Shepard A, Clary M, Ballif C, Haug F, Söderström T, Cubero O, Eminian C. Efficient nanocoax-based solar cells. *Physica Status Solidi (RRL)* 2010; **4**: 181–183.
18. Chen C, Jia R, Li HF, Meng YL, Liu XY. Electrode-contact enhancement in silicon nanowire-array-textured solar cells. *Applied Physics Letters* 2011; **98**: 143108-1–143108-3.
19. Nayak BK, Iyengar VV, Gupta MC. Efficient light trapping in silicon solar cells by ultrafast-laser- induced self-assembled micro/nano structures. *Progress in Photovoltaics: Research and Applications* 2011; **19**: 631–639.
20. Toor F, Branz HM, Page MR, Jones KM, Yuan HC. Multi-scale surface texture to improve blue response of nanoporous black silicon solar cells. *Applied Physics Letters* 2011; **99**: 103501.
21. Kumar D, Srivastava SK, Singh PK, Husain M, Kumar V. Fabrication of silicon nanowire arrays based solar cell with improved performance. *Solar Energy Materials and Solar Cells* 2011; **95**: 215–218.
22. Huang BR, Yang YK, Lin TC, Yang WL. A simple and low-cost technique for silicon nanowire arrays based solar cells. *Solar Energy Materials and Solar Cells* 2012; **98**: 357–362.
23. Liu YP, Lai T, Li HL, Wang Y, Mei ZX, Liang HL, Li ZL, Zhang FM, Wang WJ, Kuznetsov AY, Du XL. Nanostructure formation and passivation of large-area black silicon for solar cell applications. *Small* 2012; **8**: 1392–1397.
24. Lin XX, Hua X, Huang ZG, Shen WZ. Realization of high performance silicon nanowire based solar cells with large size. *Nanotechnology* 2012; **24**: 235402-1–235402-8.
25. Syu HJ, Shiu SC, Hung YJ, Hsueh CC, Lin TC, Subramani T, Lee SL, Lin CF. Influences of silicon nanowire morphology on its electro-optical properties and applications for hybrid solar cells. *Progress in Photovoltaics: Research and Applications* 2013; **21**: 1400–1410.
26. Oh J, Yuan HC, Branz HM. An 18.2%-efficiency black-silicon solar cell achieved through control of carrier recombination in nanostructures. *Nature Nanotechnology* 2012; **7**: 743–748.

27. Wang X, Peng KQ, Pan XJ, Chen X, Yang Y, Li L, Meng XM, Zhang WJ, Lee ST. High-performance silicon nanowire array photoelectrochemical solar cells through surface passivation and modification. *Angewandte Chemie International Edition* 2011; **50**: 9861–9865.
28. Kim JY, Kwon MK, Logeeswaran VJ, Grego S, Islam MS. Postgrowth in situ chlorine passivation for suppressing surface-dominant transport in silicon nanowire devices. *IEEE Transactions on Nanotechnology* 2012; **11**: 782–787.
29. Benick J, Hoex B, Van de Sanden M, Kessels WMM, Schultz O, Glunz SW. High efficiency *n*-type Si solar cells on Al_2O_3-passviated boron emitters. *Applied Physics Letters* 2008; **92**: 253504-1–253504-3.
30. Werner F, Veith B, Tiba V, Poodt P, Roozeboom F, Brendel R, Schmidt J. Very low surface recombination velocities on *p*- and *n*-type *c*-Si by ultrafast spatial atomic layer deposition of aluminum oxide. *Applied Physics Letters* 2010; **97**: 162103-1–162103-3.
31. Terlinden NM, Dingemans G, Van de Sanden MCM, Kessels WMM. Role of field-effect on *c*-Si surface passivation by ultrathin (2–20 nm) atomic layer deposited Al_2O_3. *Applied Physics Letters* 2010; **96**: 112101-1–112101-3.
32. Hoex B, Van de Sanden MCM, Schmidt J, Brendel R, Kessel WMM. Surface passivation of phosphorus-diffused n^+-type emitters by plasma-assisted atomic-layer deposited Al_2O_3. *Physica Status Solidi (RRL)* 2012; **6**: 4–6.
33. Vermang B, Goverde H, Tous L, Lorenz A, Choulat P, Horzel J, John J, Poortmans J, Mertens R. Approach for Al_2O_3 rear surface passivation of industrial *p*-type Si PERC above 19%. *Progress in Photovoltaics: Research and Applications* 2012; **20**: 269–273.
34. Lee H, Tachibana T, Ikeno N, Hashiguchi H, Arafune K, Yoshida H, Satoh S, Chikyow T, Ogura A. Interface engineering for the passivation of *c*-Si with O_3-based atomic layer deposited Al_2O_3 for solar cell application. *Applied Physics Letters* 2012; **100**: 143901-1–143901-4.
35. Wang J, Mottaghian SS, Baroughi MF. Passivation properties of atomic-layer-deposited hafnium and aluminum oxides on Si surfaces. *IEEE Transactions on Electron Devices* 2012; **59**: 342–348.
36. Saint-Cast P, Benick J, Kania D, Weiss L, Hofmann M, Rentsh J, Preu R, Glunz SW. High-efficiency *c*-Si solar cells passivated with ALD and PECVD aluminum oxide. *IEEE Electron Device Letters* 2010; **31**: 695–697.
37. Zhu LQ, Li X, Yan ZH, Zhang HL, Wan Q. Dual function of antireflectance and surface passivation of atomic-layer-deposited Al_2O_3 films. *IEEE Electron Device Letters* 2012; **33**: 1753–1755.
38. Chen C, Jia R, Yue HH, Li HF, Liu XY, Wu DQ, Ding WC, Ye TC, Kasai S, Tamotsu H, Chu JH, Wang SL. Silicon nanowire-array-textured solar cells for photovoltaic application. *Journal of Applied Physics* 2010; **108**: 094318-1–094318-5.
39. Vermang B, Goverde H, Lorenz A, Uruena A, Vereecke G, Meersschaut J, Cornagliotti E, Rothschild A, John J, Poortmans J, Mertens R. On the blistering of atomic layer deposited Al_2O_3 as Si surface passivation. *Proceedings of the 37th IEEE Photovoltaic Specialists Conference*, 2011; 003562–003567.
40. Casey HC, Fountain GG, Alley RG, Keller BP, DenBaars SP, Low interface trap density for remote plasma deposited SiO_2 on *n*-type GaN. *Applied Physics Letters* 1996; **68**: 1850–1852.
41. Werner F, Veith B, Zielke D, Kühnemund L, Tegenkamp C, Seibt M, Brendel R, Schmidt J. Electronic and chemical properties of the *c*-Si/Al_2O_3 interface. *Journal of Applied Physics* 2011; **109**: 113701-1–113701-6.